Simple scaling of catastrophic landslide dynamics

Göran Ekström and Colin P. Stark

Lamont-Doherty Earth Observatory of Columbia University, Palisades, New York, 10964, USA

One-sentence summary: *We show how the bulk dynamics of catastrophic landslides are fundamentally set by their rupture length scale though inverse modeling of teleseismic waveforms calibrated by satellite imagery.*

post-review version

Catastrophic landslides involve the acceleration and deceleration of millions of tons of rock and debris in response to the forces of gravity and dissipation. Their unpredictability and frequent location in remote areas have made observations of their dynamics rare. Through real-time detection and inverse modeling of teleseismic data we show that landslide dynamics are primarily determined by the length scale of the source mass. When combined with geometric constraints from satellite imagery, the seismically determined landslide force histories yield estimates of landslide duration, momenta, potential energy loss, mass, and runout trajectory. Measurements of these dynamical properties for 29 teleseismogenic landslides are consistent with a simple acceleration model in which height drop and rupture depth scale with the length of the failing slope.

Seismic radiation from landslides is broadband and complex (*1*). Short-period waves result from the myriad momentum exchanges taking place within the granular mass and along its sliding boundary. They are distributed in time and low in amplitude compared with the impulsive radiation associated with the sudden stress drop in tectonic earthquakes. Long-period waves radiated by landslides are simpler: they are generated by the broad cycle of unloading and reloading of the solid Earth (*2–4*) induced by the bulk acceleration and deceleration of the landslide mass. The corresponding momentum exchange is complicated by entrainment and deposition (*5–7*) during motion and by topographic undulations along the slide path (*8*). Characteristic unloading–reloading times in large landslides are several tens of seconds, making them efficient sources of seismic waves at periods of that order (*9*).

Traditional earthquake monitoring conducted by national and international agencies is designed for detection of impulsive short-period seismic waves and for location of associated tectonic earthquakes and explosions. Landslide detections are rare. A complementary method based on near-real-time data from the Global Seismographic Network (GSN) allows for the detection of seismic events through continuous back-projection of the long-period wavefield (*10–12*). This event-detection algorithm detects >90% of $M \geq 5.0$ shallow earthquakes reported by other agencies, and identifies about ten events each month that are not in other seismicity catalogues. Some of these unassociated events have been correlated with large-scale glacier calving (*13, 14*) and volcanic unrest (*15*). Here we identify and investigate another subset of these events associated with catastrophic (large and fast) landslides.

The event-detection algorithm locates events with an initial accuracy of 20–100 km (*10*). A terrestrial landslide source is established by combining this geographic location with satellite imagery, field photographs, news reports, local seismic recordings, and other sources. A comprehensive investigation of 195 unassociated detections for 2010 led to the identification of eleven major landslides (Table S1, Events 16–26). All of the seismically detected landslides

3

generated long-period surface waves roughly equivalent to a magnitude $M_{SW} \sim 5$ tectonic earthquake and all were recorded at multiple seismographic stations. Tectonically generated surface-wave signals of this magnitude are routinely used to determine earthquake fault geometries and seismic moments (*16*), suggesting that similar methods could also be used to provide a quantitative characterization of the detected landslides. For example, Kanamori and co-workers (*17, 18*) measured a subhorizontal force of $\sim 150\,s$ duration and maximum amplitude $\sim 10^{13}\,N$ associated with the massive debris avalanche following the 1980 eruption of Mount St. Helens volcano (Table S1). Seismological analyses of long-period data have usually focused on single landslide events, and typically have been limited to estimation of the average slide direction (often only in the horizontal), peak force, and duration of sliding (*19–22*). Field observations, on the other hand, frequently suggest complex three-dimensional (3-D) landslide trajectories, and numerical modeling has highlighted the effects of such complexity on the radiated seismic waves (*7, 8*).

We developed an inverse method (*12*) to infer the 3-D force sequence generated by bulk landslide motion (*23*) — from which we can deduce the trajectory of slip and dynamic properties. The new algorithm builds on and extends established methods used in earthquake analysis (*12, 16*). When applied to one of the largest landslides of 2010, this approach results in a first-order characterization of the event (Fig. 1). On January 4 of that year, our algorithm (*10, 11*) automatically detected a seismic event of long-period magnitude $M_{SW} \approx 5.3$ at 08:36 GMT and roughly located the source in northern Pakistan (Table S1). None of the international earthquake-monitoring agencies ISC, IDC, or NEIC reported this event. Following anecdotal reports that a major landslide had struck the village of Attabad that morning — blocking the Karakoram Highway, damming the Hunza river, and causing several fatalities (*24*) — we inspected long-period waveform data recorded on proximal stations and established that the seismic signal was likely caused by the Attabad slope failure. This association was confirmed by our inverse model, which provided a more accurate source location within $15\,km$ of Attabad

4

⁶⁸ and which pointed to a direction of motion down to the SSW, consistent with local reports.

⁶⁹ These reports also indicated a time of failure consistent with the seismic detection.

⁷⁰ The estimated time sequence of forces induced by acceleration of the Hunza-Attabad land-

⁷¹ slide indicates a roughly sinusoidal sequence lasting $\Delta t \sim 60\,\text{s}$ (Fig. 1a). The 3-D force vector

⁷² components vary in a synchronous fashion, which suggests a consistent azimuth of acceleration

⁷³ and deceleration and therefore a linear runout. During the first 25 s the force vector points con-

⁷⁴ sistently to the NNE with an upward vertical component, indicating reaction to acceleration of

⁷⁵ the slide mass downhill in the SSW direction. The subsequent time series reflects reversal of

⁷⁶ the force vector during deceleration, as the slide mass approached the bottom of the valley.

⁷⁷ Because the negated force history is equivalent to the rate of change of bulk landslide mo-

⁷⁸ mentum over time (*23*), its integration gives the bulk momentum over time $\mathbf{p}(t) = (m\mathbf{v})(t)$. This

⁷⁹ time series is constrained to be stationary during inversion. Assuming a constant bulk mass m

⁸⁰ over time, further integration gives the mass-scaled, 3-D vector trajectory of motion $m\mathbf{D}(t)$.

⁸¹ If an independent measure of landslide volume or mass m is available, we can divide by m to

⁸² obtain the 3-D runout $\mathbf{D}(t)$ and compare it against terrain data and post-failure imagery to test

⁸³ the validity of the inversion results and the assumption of constant mass. Alternatively, we can

⁸⁴ estimate the bulk landslide mass by comparing the mass-scaled maximum horizontal displace-

⁸⁵ ment mD_h with a center-of-mass displacement estimated from terrain data and imagery. Using

⁸⁶ the second approach, illustrated in satellite imagery of Hunza-Attabad (Fig. 1c), we estimated

⁸⁷ a horizontal center-of-mass displacement of 940 m, which gave a mass of $m \approx 1.4 \times 10^{11}\,\text{kg}$

⁸⁸ and the runout path $\mathbf{D}(t)$ shown in Fig. 1b. Evaluation in the field has estimated the deposited

⁸⁹ volume at ~ 45 million m^3 (*24*). Assuming a debris density of 2400 $\text{kg}\,\text{m}^{-3}$, this suggests a

⁹⁰ source mass of $\sim 1.1 \times 10^{11}\,\text{kg}$, broadly consistent with our estimate.

⁹¹ We applied the technique of landslide seismic detection and source inversion to a total of 29

5

events spanning 1980–2012 (Table S1). This set includes the three largest landslides of the last 33 years: Mount St. Helens in 1980 (Table S1), Kaiapit in 1988 (*25*), and Yìgòng in 2000 (*26*). Of these 29 events, 27 were recorded on global network stations while the two smallest — at Fāngtúnshān/Tàimālǐ in Taiwan (*27*) in 2009 and Akatani in Japan (*28*) in 2011 — were well recorded on regional networks. By analyzing all 29 landslides in a methodologically consistent fashion, we generated empirical constraints on catastrophic landslide dynamics spanning three orders of magnitude of failure mass that can be used with confidence in analyses of scaling (Table S1; Fig. 3).

A practical result is the logarithmic relationship (Fig. 3a) we see between the long-period magnitude M_{SW} and the maximum force F_{max}. The magnitude estimates span $M_{SW} \approx 4.6 - 5.6$ and are available only for the 27 global detections. The maximum forces here span $F_{max} \approx 4 \times 10^{10} - 5 \times 10^{12}$ N and are typically associated with the acceleration phase of the landslide. The correlation is strong, suggesting that the maximum force can be estimated from the long-period magnitude alone (to within a factor of two) and prior to waveform modeling.

We find a consistent pattern of scaling (Fig. 3b–f) among the inferred dynamic properties that can be explained with a very simple model of slope collapse and acceleration in which a single length scale L determines all the geometrical properties of the landslide source and its acceleration phase (*12*). The simple model and the inversion results indicate a linear dependence of landslide mass on maximum force $m \approx 0.54 F_{max}$ (Fig. 3b). They indicate no scaling dependence, but much variability (Fig. 3d), for peak acceleration $a \approx 2 \, \text{m}\,\text{s}^{-2}$. Observed scaling dependencies on maximum force match model deductions: peak momentum is $p_{max} \approx 27 F_{max}^{7/6}$ (Fig. 3c), potential energy loss is $\Delta E \approx 3.8 F_{max}^{4/3}$ (Fig. 3e), and runout duration is $\Delta t \approx 127 F_{max}^{1/6}$. Similarly, we find dependencies on potential energy loss such as $\Delta t \approx 110 \Delta E^{1/8}$ (Fig. 3f) and $p_{max} \approx 10 \Delta E^{7/8}$ that accord with the model. Together our results indicate peak kinetic energy is on average about 24% of potential energy loss. A practical outcome is that the mass-force

6

relation can be combined with the observed scaling between magnitude and force to provide an approximate means of estimating landslide mass (in 10^{12} kg) from long-period magnitude alone as $m \approx 0.54 \times 10^{2.2M_{SW}-12}$.

Runout duration Δt and trajectory $\mathbf{D}(t)$ inferred seismically reflect the phase of major height drop and thus significant force. For some landslides however, particularly for those running onto and down glaciers (such as Mt. Garmo (29) in 2001 and Mt. Lituya in 2012), a second longer phase of low gradient, likely low deceleration runout was mapped on imagery, but not recorded in the long-period seismicity. Such long-runout events likely indicate unusually low rates of energy dissipation as a result of frictional melting of glacial ice.

The most notable, previously undocumented landslides we identified are the seven catastrophic (M_{SW} 4.6–5.4; Table S1) events detected over four days in September 2010 and located in the eastern Karakoram. All exhibited the seismic characteristics of landslides and none were detected by earthquake monitoring agencies. Our inversions of these events indicate a common runout direction of W–WSW for all the failures, and analysis of multitemporal Landsat imagery (Fig. 2c) identified only one candidate slope failure, collapsing onto the Siachen Glacier, consistent with this time window and geographic location. Subsequent mapping using multitemporal GeoEye imagery (Fig. 2a,b) confirmed multiple failures of the northern flank of the valley.

Unlike the Mt Garmo and Mt Lituya events, runout over the Siachen glacier surface was relatively short and comparable to the height drop. Using the GeoEye imagery we estimated runout for the largest event at $D_h \approx 1320$ m and deduce the failure mass at around $m \approx 1.9 \times 10^{11}$ kg and maximum acceleration of 2.2 m s^{-2}. Because the other six events could not be tied to runout patterns in the imagery, we assumed the same maximum acceleration to calibrate their LFH inversions, yielding estimates of failure masses ranging from $m \approx 1.1 \times 10^{10}$ kg – 1.4×10^{11} kg.

This sequence of massive landsliding is an example of progressive slope failure involving multiple collapses of bedrock volumes each exceeding $10^6 - 10^7 \, \mathrm{m}^3$. While it is recognized that episodes of massive mass-wasting often comprise a hierarchy of individual landslide events, repeated similar-scale failures of the same mountain slope over mere days are more difficult to explain. In our catalogue of inversions, only the paired Randa events (*30*) in 1991 involve closely repeated failure of a similar scale at the same location. Were it not for the seismic detection, force inversion and satellite-image mapping employed here, the Siachen Glacier landslide deposit would likely be falsely interpreted as the composite of one or two extremely large failures. What is more, given its remote location it would likely have gone undetected for some time.

References

1. D. Weichert, R. B. Horner, S. G. Evans, *Bulletin of the Seismological Society of America* **84**, 1523 (1994).

2. Y. Takei, M. Kumazawa, *Geophysical Journal International* **121**, 641 (1994).

3. Y. Fukao, *Geophysical Journal International* **122**, 243 (1995).

4. M. J. McSaveney, G. Downes, *Landslides*, J. Rybar, J. Stemberk, P. Wagner, eds. (Balkema, Lisse, 2002), pp. 649–654.

5. G. B. Crosta, H. Chen, C. F. Lee, *Geomorphology* **60**, 127 (2004).

6. S. N. Ward, S. Day, *Geophysical Journal International* **167**, 991 (2006).

7. L. Moretti, *et al.*, *Geophys. Res. Lett.* **39**, L16402 (2012).

8. P. Favreau, A. Mangeney, A. Lucas, G. Crosta, F. Bouchut, *Geophysical Research Letters* **37**, L15305 (2010).

9. E. A. Okal, *J. Phys. Earth* **38**, 445 (1990).

10. G. Ekström, *Bull. Seism. Soc. Am.* **96**, 1201 (2006).

11. G. Ekström, M. Nettles, Global CMT catalog (2012). <http://globalcmt.org>.

12. See supplementary materials on *Science* Online.

13. G. Ekström, M. Nettles, G. A. Abers, *Science* **302**, 622 (2003).

14. M. Nettles, G. Ekström, *Ann. Rev. Earth Planet. Sci.* **38**, 467 (2010).

15. A. Shuler, G. Ekström, *J. Volc. Geothermal Res.* **181**, 219 (2009).

170 16. G. Ekström, M. Nettles, A. M. Dziewonski, *Phys. Earth Planet. Int.* **200–201**, 1 (2012).

171 17. H. Kanamori, J. W. Given, *Journal of Geophysical Research* **87**, 5422 (1982).

172 18. H. Kanamori, J. W. Given, T. Lay, *Journal of Geophysical Research* **89**, 1856 (1984).

173 19. H. S. Hasegawa, H. Kanamori, *Bulletin of the Seismological Society of America* **77**, 1984
174   (1987).

175 20. E. E. Brodsky, E. Gordeev, H. Kanamori, *Geophysical Research Letters* **30**, 2236 (2003).

176 21. M. La Rocca, *et al.*, *Bulletin of the Seismological Society of America* **94**, 1850 (2004).

177 22. N. A. Pino, M. Ripepe, G. B. Cimini, *Geophysical Research Letters* **31**, L02605 (2004).

178 23. W. G. Pariseau, *Engineering Geology* **16**, 111 (1980).

179 24. D. Petley, *International Water Power & Dam Construction* **63**, 27(3) (2011).

180 25. M. Peart, *Quarterly Journal of Engineering Geology* **24**, 399 (1991).

181 26. Y.-J. Shang, *et al.*, *Geomorphology* **54**, 225 (2003).

182 27. C.-H. Lin, H. Kumagai, M. Ando, T.-C. Shin, *Geophysical Research Letters* **37**, L22309
183   (2010).

184 28. M. Yamada, Y. Matsushi, M. Chigira, J. Mori, *Geophysical Research Letters* **39**, L13301
185   (2012).

186 29. V. M. Kotlyakov, *et al.*, *Materialy Gliatsiologicheskikh Issledovanii* **95**, 221 (2003).

187 30. E. Eberhardt, D. Stead, J. S. Coggan, *International Journal of Rock Mechanics and Mining*
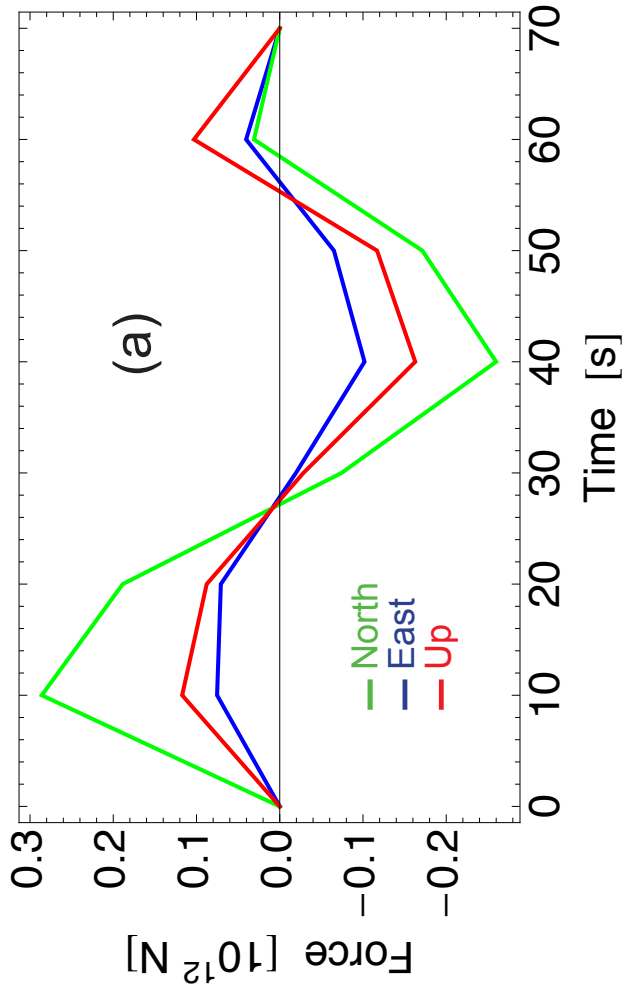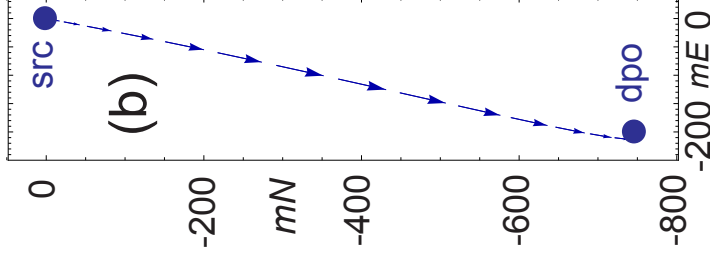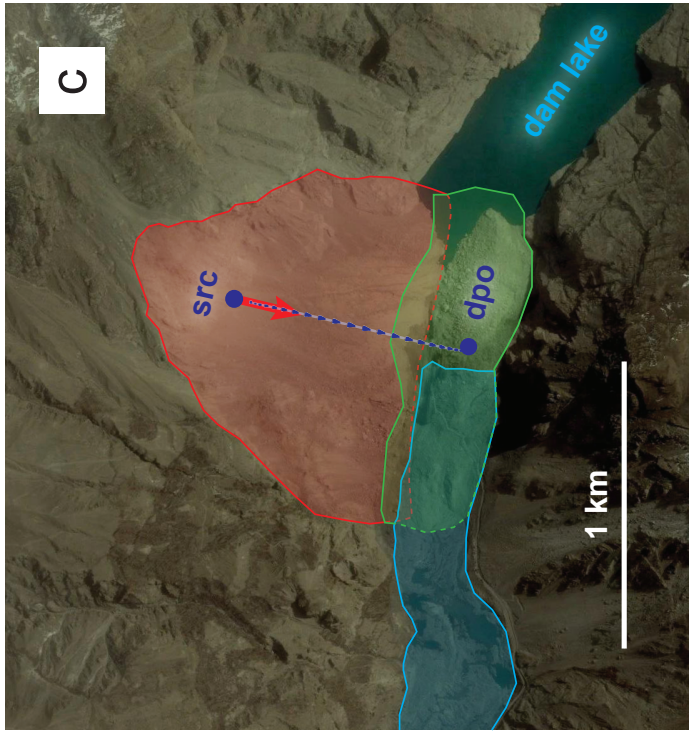188   *Sciences* **41**, 69 (2004).

Figure 1: Landslide force history and trajectory for the Hunza-Attabad landslide. (a) Inversion of the landslide force history $\mathbf{F}(t)$ (LFH) of this event, pinning the time of main failure at 08:37UT (Table S1); (b) The planform trajectory of landslide motion deduced by doubly integrating the LFH and scaling by the runout distance mapped in (c). (c) Satellite-image mapping of the landslide scar and runout. The estimated centers of the source ('src') and deposits ('dpo') are indicated; their spatial separation was used to estimate D_h, determine the effective mass, and scale the displacement trajectory $\mathbf{D}(t)$.

Figure 2: Siachen landslides, September 2010. (a) Pre- and (b) post-event GeoEye 50 cm-resolution VNIR imagery of Siachen Glacier landslide complex. (c) Inferred trajectories for the seven Siachen landslides. The slide origins were chosen to coincide, in order to illustrate the good agreement in average slide direction, with some variablility in motion in the lower portions of the trajectories. Outlined in green and yellow are the approximate source and deposit areas, respectively.

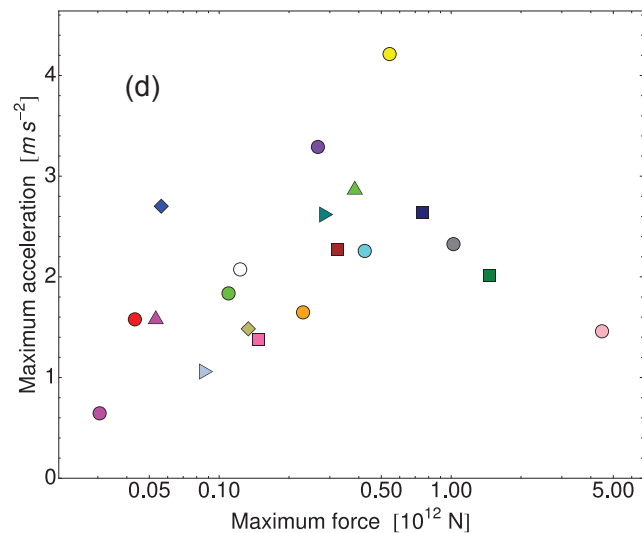**Figure 3:** Maximum force F_{max} versus (a) long-period surface-wave magnitude M_{SW}, (b) mass m, (c) maximum momentum p_{max}, (d) maximum acceleration a_{max}, and (e) potential energy loss ΔE. Runout duration Δt versus potential energy loss ΔE is shown in (f). In (a)-(c), (e), and (f), the solid lines show model fits and the dashed lines indicate model mean confidence intervals at the 99% level.

(a) Force [10^{12} N] versus Time [s] with North (green), East (blue), and Up (red) components.

(b) Horizontal force components in mN and mE, from src to dpo.

(c) Satellite image showing src, dpo, and dam lake locations with 1 km scale bar.

(a) 2009/08/04 (b) 2010/10/09 (c)

(a) $M_{sw} = 5.4 + 0.45 \log_{10}[F_{max}]$

(b) $m = 0.54\, F_{max}$

(c) $p_{max} = 27\, F_{max}^{7/6}$

(e) $\Delta E = 3.8\, F_{max}^{4/3}$

(f) $\Delta t = 110\, \Delta E^{1/8}$
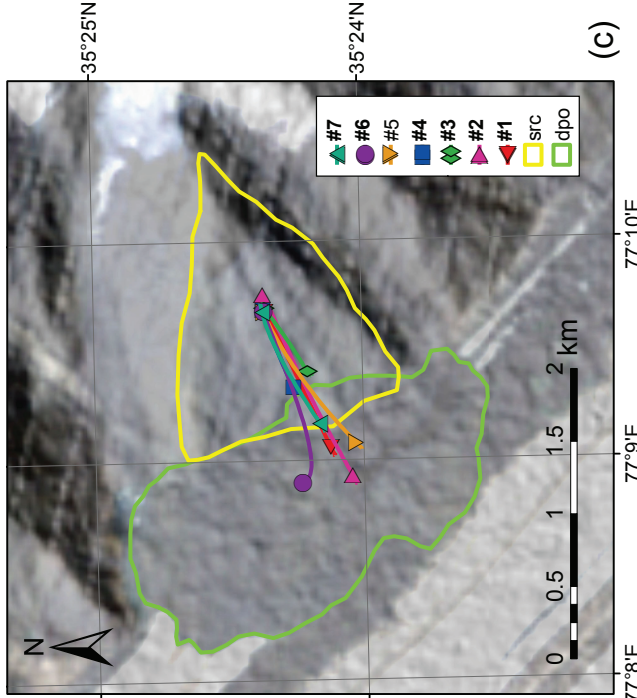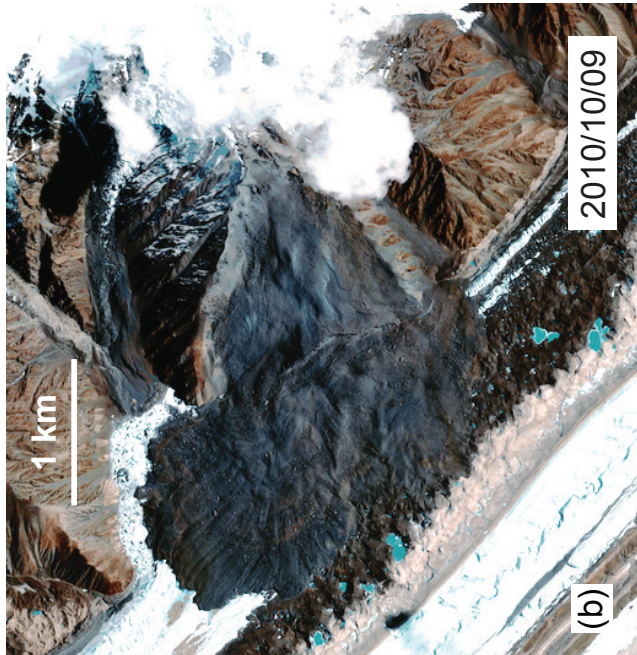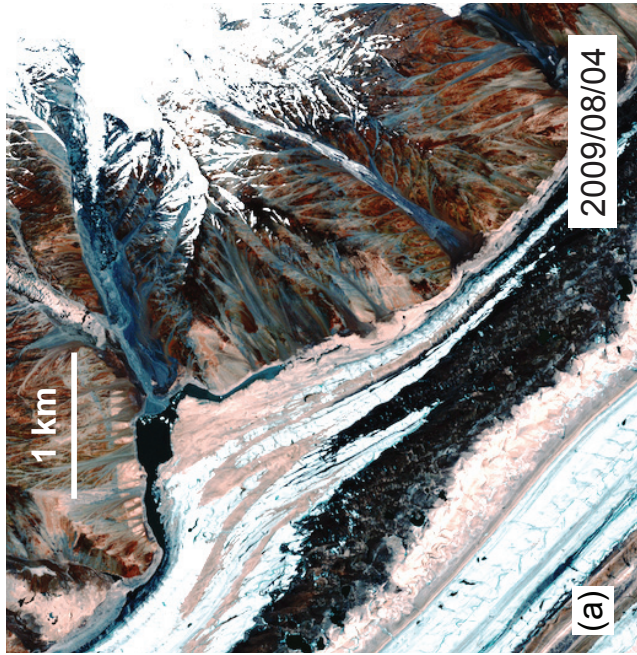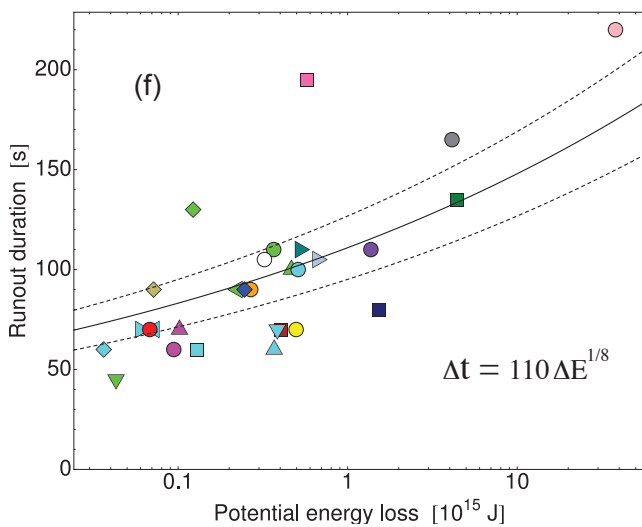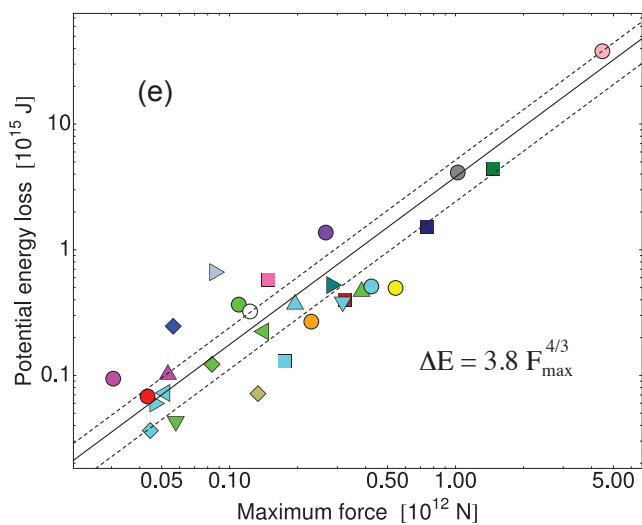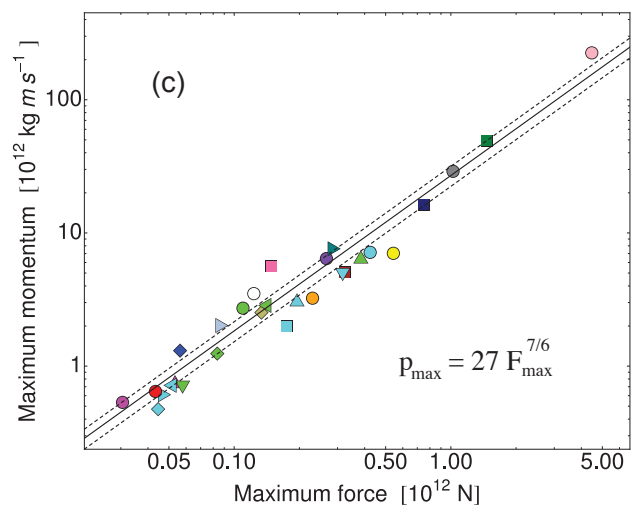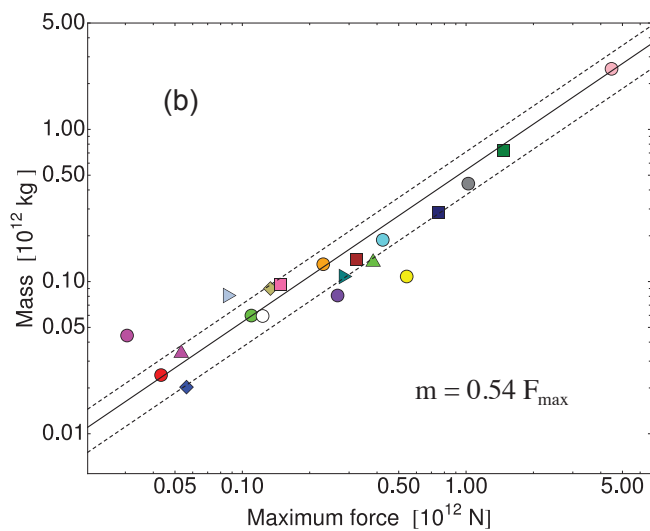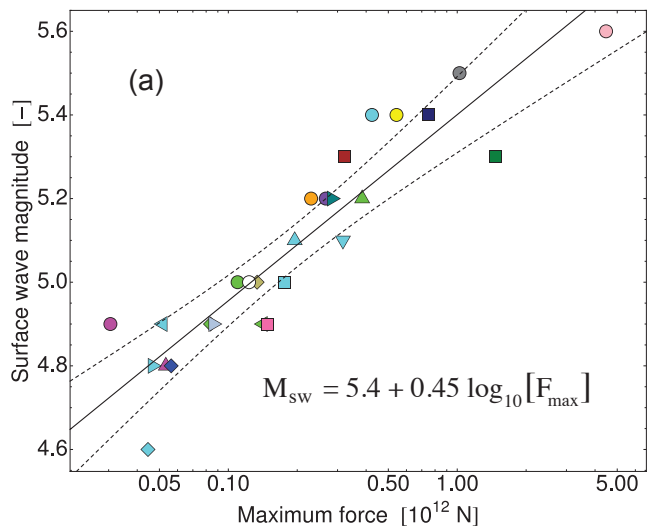
Legend:
- Mt St Helens
- Valpola
- Kaiapit
- Randa #1
- Randa #2
- Conchut
- Yigong
- Mt Garmo
- Mt Steller
- Mt Steele
- Hsiaolin
- Taoyuan
- Fangtunshan #2
- Fangtunshan #1
- Fuxing
- Hunza–Attabad
- Rio Socota
- Sheemahant
- Mt Meager
- Siachen #1
- Siachen #2
- Siachen #3
- Siachen #4
- Siachen #5
- Siachen #6
- Siachen #7
- Akatani
- Seti–Annapurna
- Mt Lituya

Axis labels:
- (a) x: Maximum force [10^{12} N]; y: Surface wave magnitude [–]
- (b) x: Maximum force [10^{12} N]; y: Mass [10^{12} kg]
- (c) x: Maximum force [10^{12} N]; y: Maximum momentum [10^{12} kg $m\,s^{-1}$]
- (d) x: Maximum force [10^{12} N]; y: Maximum acceleration [$m\,s^{-2}$]
- (e) x: Maximum force [10^{12} N]; y: Potential energy loss [10^{15} J]
- (f) x: Potential energy loss [10^{15} J]; y: Runout duration [s]

Supplementary Materials for

Simple Scaling of Catastrophic Landslide Dynamics

Göran Ekström and Colin P. Stark

correspondence to: ekstrom@ldeo.columbia.edu or cstark@ldeo.columbia.edu

This PDF file includes:

Materials and Methods

Event Detection and Location

Detection and location of seismic events that emit teleseismically detectable long-period seismic waves is accomplished using the algorithm described by Ekström *et al.* (*10*). The initial analysis makes use of seismograms collected from global networks in near-real time, and automatic results are posted on the Global CMT web site (*11*). Subsequent analysis makes use of additional archived data: typically data from 100–200 stations are included. Signals are analyzed for detections in the period band 35–150 s. The algorithm is based on a grid search of potential event locations on the surface of the Earth. For each location, the Rayleigh wave dispersion is calculated to each station. To account for the geographic heterogeneity of surface-wave phase velocities, the dispersion correction is calculated from global phase-velocity maps (*31*). The recorded signals are back-propagated to the test location by deconvolution of the propagation dispersion. The processed signals are analyzed for the simultaneous presence of coherent energy at several stations, and empirically established criteria are used to declare an event detection (*10*). A comparison based on locations of known earthquakes from the NEIC catalog shows that the surface-wave locations have median deviations from the NEIC locations of approximately 40 km (*10*). The magnitude M_{SW} of the detected event is calculated from the amplitude A of the long-period surface waves using the expression $M_{\mathrm{SW}} = c + \frac{2}{3}\log A$. The calibration factor c is determined by regression using shallow earthquakes with known moment magnitudes (*10*).

Landslide Force Inversion

The seismic waves generated by a landslide source are caused by time-varying forces acting on the Earth. We follow the approach developed by Kanamori *et al.* (*18*) and consider the sliding mass a separate body from the solid Earth. The momentum change of the slide is equivalent to a force $\mathbf{F}_{\mathrm{S}} = \mathrm{d}(m\mathbf{v})/\mathrm{d}t$, where m is the mass of the slide and $\mathbf{v}$ is the velocity of the slide. The forces acting on the slide mass are gravity, friction, and centripetal forces, and each of these has a reactive counterpart acting on the solid earth in an opposite direction. The landslide therefore exerts a force on the solid Earth

$$\mathbf{F}[\mathbf{x},t] = -\mathbf{F}_{\mathrm{S}} = -\frac{\mathrm{d}(m\mathbf{v})}{\mathrm{d}t}[\mathbf{x},t]. \tag{1}$$

In simple terms, as the landslide mass accelerates and then decelerates down slope it effectively unloads and then reloads the hillslope, and this variable loading of the elastic solid Earth generates seismic waves.

In practice we cannot resolve the spatial distribution of the force and we parameterize $\mathbf{F}$ as a bulk-average, time-varying point force acting on the Earth's surface. This is justified to the extent that the spatial scale of the slide is small compared with the wavelength of the seismic waves and with the distances to the recording seismic stations. The seismic radiation from the torque exerted by the slide mass is weak for the type of seismic waves considered here (*20*),

2

and we do not include this contribution to the landslide seismograms. Analysis is restricted to long-period waves with $T \geq 30\,\mathrm{s}$ since the unloading/loading cycle, i.e., the duration of slip, is of that order (Table S2), such that the bulk of the seismic wave energy is radiated at long periods.

We parameterize the time-varying force as a sequence of partially overlapping isosceles triangles with a half-width appropriate for resolving the complexity seen in the seismograms — typically 10 to 15 s. Synthetic seismograms are calculated by summation of the Earth's elastic normal modes using the PREM Earth model (*32*) and corrections for Earth's laterally heterogeneous crust and mantle (*16*). We solve for the amplitudes of the triangles that define the time histories of each component of the force (up, north, east) by minimizing, in a least-squares sense, the misfit between observed and corresponding synthetic seismograms. The time history of each force component is constrained to integrate to zero to satisfy the physical condition that the sliding mass is at rest before and after the landslide. A weak smoothness constraint is also applied, which eliminates rapid oscillations in the force-time histories. We also solve for the best-fit point-source location of the landslide source. Inversion for the force parameters is performed using a modified version of the centroid-moment-tensor (CMT) algorithm (*33*).

An example of the data used and the match between observed and model seismograms for the Hunza-Attabad landslide (*24*) (Table S1) is shown in Figure S1. The closest station used in the analysis was KBL in Kabul, Afghanistan at a distance of $\sim$600 km. The GSN station in Nilore, Pakistan was not operating at the time of the landslide.

The relationship between the estimated forces on the Earth and the dynamic parameters of the slide mass is written

$$\mathbf{I}[t] = -(m\mathbf{v})[t] = \int_0^t \mathbf{F}[\tau]\,\mathrm{d}\tau \tag{2}$$

where $\mathbf{I}[t]$ is the impulse acting on the Earth and $-(m\mathbf{v})[t]$ is the momentum of the slide mass. Integrating the force a second time, we obtain an expression for the trajectory, which, if a fixed reference slide mass m_0 is chosen, can be written

$$\mathbf{D}[t] = -\frac{1}{m_0}\int_0^t \mathbf{I}[\tau]\,\mathrm{d}\tau \tag{3}$$

where $\mathbf{D}[t]$ is the time-varying displacement of the center of mass.

The trade-off that exists between mass and displacement in this point-source representation is apparent. However, if the final displacement $\mathbf{D}[t \to \infty]$ of the sliding mass is known from independent observations, the equation shows that a representative slide mass can be estimated from the seismically determined forces (Table S1). Alternatively, if the slide mass is known, the acceleration, speed, and slide trajectory can be determined from the forces.
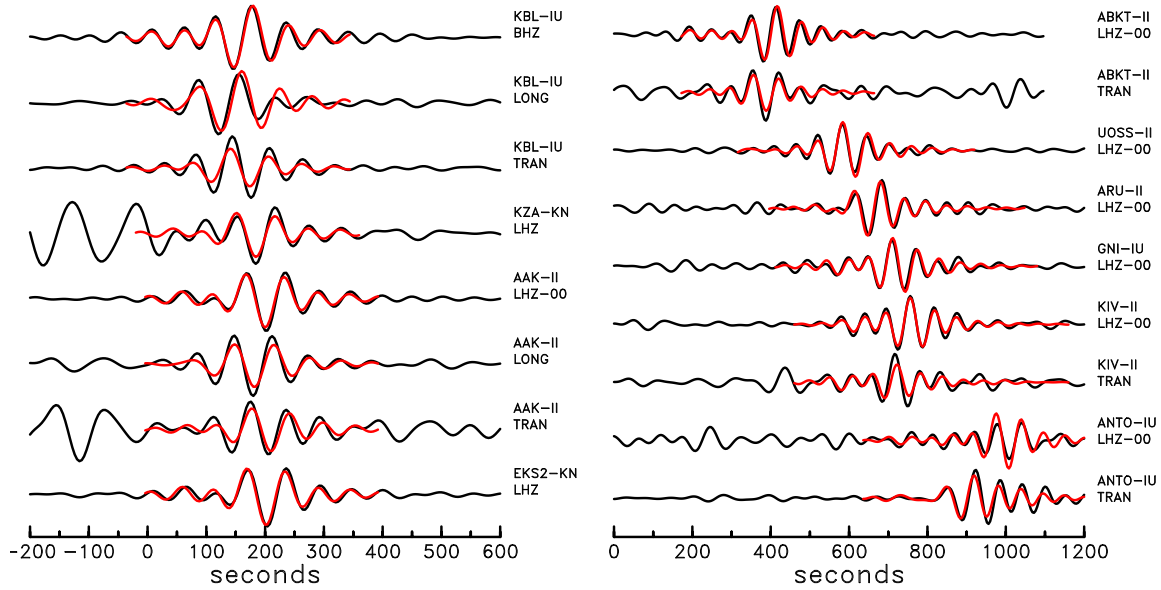
Figure S1: Comparison of observed seismograms (black) recorded at several stations of the Global Seismographic Network and the Kyrgyzstan Seismic Network and corresponding predicted waveforms (red) calculated for the best-fitting source model for the Hunza-Attabad landslide. The seismograms were filtered between 50 s and 150 s period using a phase-free (acausal) band-pass filter. The time scale (horizontal axis) is with reference to the teleseismically determined origin time of the landslide. The station and channel names are given to the right of each seismogram pair. The channel name LHZ/-LHZ-00 refers to the vertical channel, and LONG and TRAN refer to longitudinal and transverse motion at the station, obtained by rotation of the horizonal seismometer channels.

4

Supplementary Text

Model of Slope Collapse and Acceleration

The central model premise is that one length scale L determines all the key geometric properties of the landslide source and its acceleration phase: (i) we assume that the slide geometry is self-similar (*34, 35*), that variations in the density of collapsed material are minor, and that entrainment (bulking) need not be considered, such that source mass scales with volume and thus as $m \sim L^3$; (ii) the angle of slope failure may vary but is assumed independent of landslide size, such that the initial height drop scales with the landslide length $H \sim L$; (iii) the travel distance downslope to the transition point between acceleration and deceleration is assumed variable but proportional to the initial height drop, and runout duration is assumed tied to acceleration duration, such that runout lasts $\Delta t \propto \sqrt{2L/a}$. The model predicts that the peak force should scale as $F_{\mathrm{max}} \sim L^3$ and runout duration as $\Delta t \sim L^{1/2}$. Impulse is the integral of force over time, equivalent to $F_{\mathrm{max}}\Delta t$, implying that peak momentum should scales as $p_{\mathrm{max}} \sim L^{7/2}$. Similarly, the maximum speed should scale as $|\mathbf{v}|_{\mathrm{max}} \sim L^{1/2}$. Integrating the vertical force component twice suggests that the potential energy loss should scale as $\Delta E \sim L^4$.

Constraints on volume, mass and runout distance

Published values for landslide source volume and runout distance are available for the several of the landslides studied here (Table S1). In some cases, source mass estimates have also been published; in others, mass can be estimated given knowledge or assumption of mean source density. For most of the events analyzed here, such mass estimates were used to disambiguate the inverted, mass-scaled trajectories (Materials and Methods): Mt St Helens (*6, 17, 18, 36, 37*); Valpola (*5, 38, 39*); Kaiapit (*25, 40*); Randa (*30, 41*); Yìgòng (*26, 42, 43*); Mt Garmo (*29, 44*); Mt Steller (*7*); Mt Steele (*45*); Xiǎolín (*27, 46, 47*); Hunza-Attabad (*24, 48*); Mt Meager (*49, 50*); Akatani (*28*). At present there are no published constraints on the erosion volumes or runout geometry of the following events: Conchut, Rio Sócota, Sheemahant, the set of Siachen failures, Seti-Annapurna and Mt Lituya. Several seismic detections of the 2010 Typhoon Morakot-triggered events (Fāngtúnshān, Fùxíng, and Táoyuán) have been published (*27*) but without estimates of erosion mass or runout geometry.

No.	Name	Date UT	Time UT	Location °N	°E	M_{SW} -	F_{max} 10^{12} N	p_{max} 10^{12} kg m s^{-1}	ΔE 10^{15} J	Δt s	m 10^{12} kg	D_z m	D_h m	$|v|_{max}$ m s^{-1}
1	Mt St Helens	1980/05/18	15:32	46.21	-122.19	5.6	4.470	225.00	38.000	220	2.500	1549	7753	90.0
2	Valpola	1987/07/28	05:24	46.38	10.34	5.4	0.543	7.03	0.497	70	0.108	469	1441	65.1
3	Kaiapit	1988/09/06	00:42	-6.12	146.30	5.3	1.470	49.10	4.420	135	0.729	618	4512	67.3
4	Randa #1	1991/04/18	04:41	46.11	7.77	4.9	0.031	0.53	0.094	60	0.044	217	277	12.1
5	Randa #2	1991/05/09	18:52	46.11	7.77	4.8	0.053	0.74	0.102	70	0.034	307	646	21.8
6	Conchut	1999/11/07	18:03	-6.41	-78.47	5.0	0.134	2.52	0.072	90	0.090	81	1219	28.1
7	Yigòng	2000/04/09	12:00	30.24	94.99	5.5	1.020	29.00	4.120	165	0.440	955	5229	65.9
8	Mt Garmo	2001/09/02	16:57	38.79	72.08	5.4	0.749	16.20	1.520	80	0.284	547	2190	57.3
9	Mt Steller	2005/09/14	19:59	60.52	-143.09	5.2	0.267	6.42	1.370	110	0.081	1725	3275	79.3
10	Mt Steele	2007/07/25	00:57	61.11	-140.30	5.2	0.283	7.60	0.523	110	0.108	494	3354	70.4
11	Hsiàolín	2009/08/08	22:16	23.17	120.65	5.0	0.110	2.72	0.366	110	0.060	624	2253	45.5
12	Táoyuán	2009/08/09	02:52	23.22	120.76	4.9	0.142	2.85	0.224	90	0.252	91	393	11.3
13	Fàngtúnshān #2	2009/08/09	09:32	22.56	120.81	5.2	0.384	6.36	0.466	100	0.134	354	1933	47.4
14	Fàngtúnshān #1	2009/08/09	09:32	22.56	120.81	-.-	0.058	0.72	0.043	45	0.013	337	1116	55.4
15	Fùxīng	2009/08/10	11:06	23.23	120.76	4.9	0.084	1.24	0.123	130	0.052	240	959	23.9
16	Hunza-Attabad	2010/01/04	08:36	36.31	74.82	5.3	0.323	5.07	0.402	70	0.140	292	938	36.2
17	Rio Sócota	2010/02/20	18:01	-6.30	-78.60	5.2	0.230	3.24	0.268	90	0.130	210	673	24.9
18	Sheemahant	2010/07/09	07:35	51.87	-125.95	4.9	0.086	2.02	0.664	105	0.081	835	1084	24.9
19	Mt Meager	2010/08/06	10:29	50.62	-123.50	4.9	0.148	5.60	0.576	195	0.096	612	4553	58.3
20	Siachen #1	2010/09/09	01:18	35.41	77.16	4.9	0.052	0.72	0.072	70	0.023	322	1165	31.3
21	Siachen #2	2010/09/09	01:41	35.41	77.16	4.8	0.047	0.61	0.060	70	0.011	557	1405	55.7
22	Siachen #3	2010/09/12	10:00	35.41	77.16	4.6	0.045	0.48	0.036	60	0.020	188	608	24.1
23	Siachen #4	2010/09/12	11:17	35.41	77.16	5.0	0.175	1.99	0.129	60	0.078	170	670	25.6
24	Siachen #5	2010/09/12	11:23	35.41	77.16	5.1	0.317	5.05	0.384	70	0.140	279	1223	36.0
25	Siachen #6	2010/09/12	20:37	35.41	77.16	5.4	0.424	7.15	0.511	100	0.188	277	1319	38.0
26	Siachen #7	2010/09/12	20:50	35.41	77.16	5.1	0.195	3.03	0.369	60	0.086	435	983	35.1
27	Akatani	2011/09/04	07:22	34.12	135.72	-.-	0.043	0.64	0.068	70	0.024	285	576	26.6
28	Seti-Annapurna	2012/05/05	03:24	28.53	84.06	5.0	0.123	3.50	0.323	105	0.059	554	2745	59.0
29	Mt Lituya	2012/06/11	22:23	58.80	-137.43	4.8	0.056	1.31	0.246	90	0.020	1239	2407	64.5

Table S1. Date and time are given in UT (GMT), and result from the seismic detection and analysis. Location refers to the center of the landslide as identified in imagery data. M_{SW} is the magnitude estimate from the long-period detection (*10*), when available. F_{max} and p_{max} are the maximum absolute force and momentum during the slide motion, and ΔE is the total potential energy change obtained by integrating the vertical component of the LFH. Δt is the total duration in the LFH inversion. The column labeled m gives the mass estimate obtained as a result of dividing the mass-distance product by the observed runout distance. D_z and D_h are the vertical and horizontal components of the LFH-estimated, total mass-center displacement; $|v|_{max}$ is the speed obtained by dividing p_{max} by m.

6

References

1. D. Weichert, R. B. Horner, S. G. Evans, *Bulletin of the Seismological Society of America* **84**, 1523 (1994).

2. Y. Takei, M. Kumazawa, *Geophysical Journal International* **121**, 641 (1994).

3. Y. Fukao, *Geophysical Journal International* **122**, 243 (1995).

4. M. J. McSaveney, G. Downes, *Landslides*, J. Rybar, J. Stemberk, P. Wagner, eds. (Balkema, Lisse, 2002), pp. 649–654.

5. G. B. Crosta, H. Chen, C. F. Lee, *Geomorphology* **60**, 127 (2004).

6. S. N. Ward, S. Day, *Geophysical Journal International* **167**, 991 (2006).

7. L. Moretti, *et al.*, *Geophys. Res. Lett.* **39**, L16402 (2012).

8. P. Favreau, A. Mangeney, A. Lucas, G. Crosta, F. Bouchut, *Geophysical Research Letters* **37**, L15305 (2010).

9. E. A. Okal, *J. Phys. Earth* **38**, 445 (1990).

10. G. Ekström, *Bull. Seism. Soc. Am.* **96**, 1201 (2006).

11. G. Ekström, M. Nettles, Global CMT catalog (2012). `<http://globalcmt.org>`.

12. See supplementary materials on *Science* Online.

13. G. Ekström, M. Nettles, G. A. Abers, *Science* **302**, 622 (2003).

14. M. Nettles, G. Ekström, *Ann. Rev. Earth Planet. Sci.* **38**, 467 (2010).

15. A. Shuler, G. Ekström, *J. Volc. Geothermal Res.* **181**, 219 (2009).

16. G. Ekström, M. Nettles, A. M. Dziewonski, *Phys. Earth Planet. Int.* **200–201**, 1 (2012).

17. H. Kanamori, J. W. Given, *Journal of Geophysical Research* **87**, 5422 (1982).

18. H. Kanamori, J. W. Given, T. Lay, *Journal of Geophysical Research* **89**, 1856 (1984).

19. H. S. Hasegawa, H. Kanamori, *Bulletin of the Seismological Society of America* **77**, 1984 (1987).

20. E. E. Brodsky, E. Gordeev, H. Kanamori, *Geophysical Research Letters* **30**, 2236 (2003).

21. M. La Rocca, *et al.*, *Bulletin of the Seismological Society of America* **94**, 1850 (2004).

7

22. N. A. Pino, M. Ripepe, G. B. Cimini, *Geophysical Research Letters* **31**, L02605 (2004).

23. W. G. Pariseau, *Engineering Geology* **16**, 111 (1980).

24. D. Petley, *International Water Power & Dam Construction* **63**, 27(3) (2011).

25. M. Peart, *Quarterly Journal of Engineering Geology* **24**, 399 (1991).

26. Y.-J. Shang, *et al.*, *Geomorphology* **54**, 225 (2003).

27. C.-H. Lin, H. Kumagai, M. Ando, T.-C. Shin, *Geophysical Research Letters* **37**, L22309 (2010).

28. M. Yamada, Y. Matsushi, M. Chigira, J. Mori, *Geophysical Research Letters* **39**, L13301 (2012).

29. V. M. Kotlyakov, *et al.*, *Materialy Gliatsiologicheskikh Issledovanii* **95**, 221 (2003).

30. E. Eberhardt, D. Stead, J. S. Coggan, *International Journal of Rock Mechanics and Mining Sciences* **41**, 69 (2004).

31. G. Ekström, J. Tromp, E. W. F. Larson, *J. Geophys. Res.* **102**, 8137 (1997).

32. A. M. Dziewonski, D. L. Anderson, *Physics of the Earth and Planetary Interiors* **25**, 297 (1981).

33. A. M. Dziewonski, T.-A. Chou, J. H. Woodhouse, *Journal of Geophysical Research* **86**, 2825 (1981).

34. N. Hovius, C. P. Stark, P. A. Allen, *Geology* **25**, 231 (1997).

35. F. Guzzetti, F. Ardizzone, M. Cardinali, M. Rossi, D. Valigi, *Earth Planet. Sci. Lett.* **279**, 222 (2009).

36. R. W. Burger, C. A. Langston, *Journal of Geophysical Research* **90**, 7653 (1985).

37. B. Voight, H. Glicken, R. J. Janda, P. M. Douglass, *Catastrophic rockslide-avalanche of May 18, the 1980 eruptions of Mount St. Helens* (U.S. Geol. Survey, Washington D.C., 1981), vol. 1250 of *U.S. Geological Survey Professional Paper*, pp. 347–378.

38. G. B. Crosta, S. Imposimato, D. G. Roddeman, *Natural Hazards and Earth System Sciences* **3**, 523 (2003).

39. G. B. Crosta, P. Frattini, N. Fusi, *Journal of Geophysical Research* **112**, F01006 (2007).

40. M. Drechsler, I. Ripper, E. Rooke, E. Warren, *Engineering Geology in Tropical Terrains*, Technical sub-committee of EGITT, ed. (Universiti Kebangsaan, Malaysia, 1989), pp. 1–10.

8

41. D. Stead, E. Eberhardt, J. S. Coggan, *Engineering Geology* **83**, 217 (2006).

42. Z.-H. Wang, J.-T. Lu, *Earth Observing Systems VII*, W. L. Barnes, ed. (2002), vol. 4814 of *Proceedings of SPIE*, pp. 34–38.

43. C.-H. Zhou, Z.-Q. Yue, C.-F. Lee, B.-Q. Zhu, Z.-H. Wang, *Quarterly Journal of Engineering Geology and Hydrogeology* **34**, 325 (2001).

44. D. Schneider, C. Huggel, W. Haeberli, R. Kaitna, *Earth Surface Processes and Landforms* **36**, 1948 (2011).

45. P. S. Lipovsky, *et al.*, *Landslides* **5**, 445 (2008).

46. C.-Y. Kuo, *et al.*, *Journal of Geophysical Research* **116**, F04007 (2011).

47. C.-L. Tang, *et al.*, *Engineering Geology* **106**, 1 (2009).

48. J. F. J. Shroder, *Geomorphology* **26**, 81 (1998).

49. R. H. Guthrie, *et al.*, *Natural Hazards and Earth System Sciences* **12**, 1277 (2012).

50. C. Huggel, J. J. Clague, O. Korup, *Earth Surface Processes and Landforms* **37**, 77 (2012).